Supporting Material

Brownian dynamics of subunit addition-loss kinetics and thermodynamics in linear polymer self-assembly

Brian T. Castle and David J. Odde
Department of Biomedical Engineering, University of Minnesota, Minneapolis, MN 55455

CONTENTS

Supporting Methods

Simulation procedure

For all simulations we implemented the following procedure:

1. Initialize microtubule structure, as well as the starting position and orientation of the freely diffusing unit.
2. Translate and rotate the free unit.
3. Implement Metropolis Monte Carlo criterion based on the current and projected energetic states.
4. Check ending criteria for the given simulation (binding state or separation). If satisfied, continue to step 5 otherwise return to step 2.
5. Calculate the rate.

At each time step, subunits experienced a translational-rotational displacement described by

$$\mathbf{v} = (\Delta x_1', \Delta x_2', \Delta x_3', \phi_1, \phi_2, \phi_3), \tag{S1}$$

where $\Delta x_1'$, $\Delta x_2'$, and $\Delta x_3'$ are translational displacements of the centroid position in the subunit body frame and ϕ_1, ϕ_2, and ϕ_3 are rotations of the body frame axes about the lab frame axes. Each translational displacement was sampled from a Gaussian distribution that obeys

$$\left\langle (\Delta x_k')^2 \right\rangle = 2D\Delta t \tag{S2}$$

where D is the translational diffusion coefficient parallel ($D_{\parallel}$, for k=1) or perpendicular ($D_{\perp}$, for k=2,3) to the long axis of an ellipsoid (1) and Δt is the current time step. Similar distributions were used to generate rotational displacements with D replaced by the respective rotational diffusion coefficient for axial (D_a, for k=1) or non-axial rotation (D_r, for k=2,3). Centroid displacements in the body frame were translated to the lab frame as described by (2). At each time point

$$\begin{bmatrix} \Delta x_1 \\ \Delta x_2 \\ \Delta x_3 \end{bmatrix} = \mathbf{M}(t_j) \cdot \begin{bmatrix} \Delta x_1' \\ \Delta x_2' \\ \Delta x_3' \end{bmatrix}, \tag{S3}$$

where $\mathbf{M}(t_j)$ is a three-dimensional rotation matrix that defines the rotation of the body frame axes about each individual axis of the lab frame at the current time step. The matrix $\mathbf{M}(t_j)$ is updated after each accepted step using the random rotational displacements according to

$$\mathbf{M}(t_{j+1}) = \mathbf{M}(t_j) \cdot \mathbf{R}(\phi_1, \phi_2, \phi_3) = \mathbf{M}(t_j) \cdot \mathbf{R}_3 \cdot \mathbf{R}_2 \cdot \mathbf{R}_1, \tag{S4}$$

where $\mathbf{R}_1$, $\mathbf{R}_2$, and $\mathbf{R}_3$ are the respective rotation matrices about each lab frame axis, for example

$$\mathbf{R}_1 = \begin{bmatrix} 1 & 0 & 0 \\ 0 & \cos(\phi_1) & -\sin(\phi_1) \\ 0 & \sin(\phi_1) & \cos(\phi_1) \end{bmatrix}. \tag{S5}$$

To minimize the number of steps when a free unit was not near the microtubule lattice, we used a variable time step that was based on the separation distance between paired binding zones. At each time point, the time step was calculated from

$$\Delta t = \frac{1}{6D_{\|}}\left(\frac{d}{\lambda}\right)^2, \tag{S6}$$

such that the root-mean-squared displacement for a given time step was less than the distance between interacting zones. In Eq. S6 above, d is defined as the minimum separation distance between corresponding interaction zones ($d = \min[r_1(t_j), r_2(t_j), r_3(t_j)]$) unless $d < r_B$, then $d = r_B$, such that the $\min(\Delta t) > 1$ ps. We used the diffusion coefficient along the long axis of the super-ellipsoid ($D_{\|}$) in Eq. S6, as this was the larger of the two translational diffusion coefficients in the body frame. An adjustable constant, λ, is used to scale the size and number of steps taken during the simulation. When subunits were far away from the lattice (> 100 nm) λ = 5, otherwise λ = 10 for all simulations. Using these values of λ ensured that energy changes of bound zones were relatively small (average $|\Delta U| < 1.0\ k_B T$) while still minimizing simulation time.

Before advancing to the next time point, attempted steps were either allowed or disallowed through implementation of Metropolis Monte Carlo (3), where $P_{step} = \min[1,\exp(-\Delta U/k_B T)]$. Here favorable steps ($\Delta U \leq 0$) are always allowed and unfavorable steps ($\Delta U > 0$) are accepted according to Boltzmann's law. When a freely diffusing subunit spatially overlaps the microtubule lattice, we assumed that $\Delta U = \infty$ (such that $P_{step} = 0$) to implement hard sphere rejection criteria. In the case of a rejected step, time is advanced by Δt but the position and orientation of the diffusing unit does not change from the previous time point. While the implementation of a variable time step and sampling moves from a Gaussian random variable were modifications to previous versions of the Metropolis algorithm for protein dynamics (4, 5), we found that this algorithm converged to theoretical expectation both in the presence and absence of an external force (Fig. S1; see also Supporting Results and Discussion) while enabling faster simulation.

Estimating on-rate constants

To isolate potential effects on both diffusion-limited arrivals to the microtubule lattice and binding, we split simulations into two parts, far- and near-field. Rates for each simulation scale were calculated according to (6) as

$$k = \frac{k_D(R_{start})\beta}{1-(1-\beta)k_D(R_{start})/k_D(R_{end})}, \tag{S7}$$

where $k_D(R)$ is the diffusion-limited rate of arrival to a center-to-center distance of R defined by

$$k_D(R) = 4\pi D_{avg} R \tag{S8}$$

Here, D_{avg} is the average diffusion coefficient in three body axes of the ellipsoid from

$$D_{avg} = (2D_{\perp} + D_{\|})/3 \tag{S9}$$

In far-field simulations (diffusion-limited arrivals), freely diffusing subunits are initiated by placement on a spherical surface of radius R_{start} = 400 nm and with a random orientation. Subunits are allowed to diffuse until reaching either R_{end} = 3200 nm (i.e. they diffused far away from the binding site and were highly unlikely to bind) or a center-to-center distance of 10 nm from the subunit of interest within the microtubule lattice (i.e. they diffused close to the binding site and were potentially capable of binding). Here, β in Eq. S7 is the fraction of diffusing units that reach 10 nm center-to-center before reaching R_{end}. Therefore, k is the diffusion-limited arrival rate to a center-to-center distance of 10 nm ($k_D(R = 10\text{ nm})$). The centroid positions of units that reach 10 nm are subsequently used as the starting positions to initiate the corresponding near-field simulations. In the near-field simulations R_{end} = 400 nm (value of R_{start}

for far-field) and $k_D(R_{start})$ in Eq. S7 is replaced by the estimated value of $k_D(R = 10$ nm) from the corresponding far-field simulations. For near-field simulations, β is the fraction of subunits that completely bind, or meet the criteria that all individual zones (either longitudinal, lateral, or both) are within the binding radius ($r_i <= r_B$ for all values of i). Eq. S7 then gives the estimated association rate constant ($k_{on,PF}$) for binding to the protofilament of interest. For each binding site condition, we ran a total of 500,000 far-field and 200,000 near-field simulations, which required about 50 CPU hours/processor.

Defining a distance criterion for unbinding events

Defining when a subunit is unbound is not as straightforward as defining when it is bound. As seen in Fig. S3A, freely diffusing subunits break all zone contacts ($N = 0$, $r_i > r_B$ for all i) multiple times before finally diffusing away from the microtubule lattice. This is because when a free unit first breaks all contacts, it is still highly correlated with its bound orientation, making the probability of rebinding very high. It is difficult to reason that this is a true unbinding event because the majority will immediately rebind (Fig. S3). Thus, to more appropriately define an unbinding event we used a separation distance criterion, similar to (7), where the unbinding radius (R_U) is greater than the binding radius (r_B) (Note: we can not directly compare r_B and R_U, as r_B is an edge-to-edge distance and R_U is center-to-center). To determine this distance, we simulated completely bound subunits until they reached varying center-to-center separation distances (R) from their binding partner. The resulting centroid positions and subunit orientations were then used to initiate subsequent binding simulations to estimate the probability of rebinding. We define R_U as the distance where a free unit has a low probability ($p < 0.01$) of rebinding before diffusing away, $R_U = 11$ nm center-to-center in this case (Fig. S3B). Using our distance criterion for unbinding, the distribution of unbinding times fits well with the expected single exponential ($p = 0.82$, Kolmogorov-Smirnov test) for a first-order rate (Fig. S3C). Therefore, we reason that this distance criterion is a reasonable way to practically define when a freely diffusing subunit is unbound within the simulation.

We did not simulate complete unbinding events in the very stable condition where a subunit has a longitudinal bond and two lateral bonds, due to the expected duration of the interaction (from (8), $k_{off} = 0.05$ s^{-1} for $k_{on,PF} = 4$ μM^{-1}s^{-1}). Alternatively, we set a limit for the unbinding time, τ, and looked at the number of successful unbinding events in that amount of time. The number of successes will obey a binomial distribution, with probability of success $p = k/n$ where k is the number of successes and n is the total number of simulations. Since the unbinding time is exponentially distributed (Fig. S3C), the probability that an event occurs in $T <= \tau$ is $p = 1\text{-}e^{-\lambda\tau}$. From this we obtain $k/n = 1\text{-}e^{-\lambda\tau}$ and thus can estimate the rate, λ, from the number of successes and the cut-off time. Setting a limit of $\tau = 1$ms, we found that zero subunits successfully unbound for conditions with one longitudinal and two lateral bonds for both tubulin and actin. Therefore we set an upper limit on the off-rate by finding the maximum value of λ, such that the probability of observing zero success in n trials for the binomial $B(n, p = 1\text{-}e^{-\lambda\tau})$ was greater than 0.05.

Simulation of microtubule net assembly

Net assembly of individual microtubules was simulated according to (8) at 6.5 μM free tubulin concentration for three penalty conditions: without penalties, two-neighbor penalty only (9), and model estimated penalties for one and two lateral neighbors. Simulations in each

condition were run for a total of 60 s of real-time and the resulting tip structures from the last 30s were examined at 1s intervals. A total of 16 runs were performed, resulting in 496 structures per condition. The zero-neighbor on-rate constant ($k_{on,PF}$) was scaled in simulations with penalties such that the average microtubule on-rate constant ($k_{on,MT}$) was equal for all simulations. Additionally, we increased the strength of the longitudinal bond in simulations with penalties (more negative ΔG^0_{long}; -0.4 k_BT or -1.0 k_BT for simulations with only two-neighbor and with both penalties, respectively) such that the net assembly rate was equal in each condition. Resulting structures from each simulation condition were ordered by the standard deviation of protofilament lengths, then the lower and upper 10% were considered to be blunt and tapered for that condition, respectively. This parsing of the tip structures was performed for each condition individually in order to compare the fraction of protofilaments with zero, one, or two lateral neighbors in the blunt and tapered tips across simulation conditions.

Supporting Results and Discussion

Comparing the modified Metropolis Monte Carlo to previous methods

In the presence of an external force, our simulation approach is based on the Metropolis Monte Carlo (3) (MMC) method for protein dynamics. The MMC method is a solution for the diffusive Fokker-Plank equation

$$\frac{\partial p(x,t)}{\partial t} = D\frac{\partial^2 p(x,t)}{\partial x^2} - \frac{1}{\gamma}\frac{\partial}{\partial x}[F(x)p(x,t)] \quad \text{(S10)}$$

when molecule steps are sampled from a uniform distribution [-*r*,*r*], where *r* is small and held constant throughout the simulation (4, 5). We implemented the following two modifications, which serve to improve algorithm efficiency without a substantial cost in accuracy (documented below): 1) steps were sampled from a Gaussian distribution instead of a uniform distribution, and 2), the time step varies throughout the simulation such that time steps are larger when the diffusing tubulin subunit is far from the binding site on the microtubule. Since our algorithm has been modified from the original MMC, we simulated a number of asymptotic cases that have analytical solutions to Eq. S10 to confirm that our modified MMC yields the correct solutions (4, 5).

Assuming a delta function initial condition $p(x,t = 0) = \delta(x\text{-}x_0)$ at $x_0 = 0$, solutions to Eq. S10 are well defined in both the presence and absence of an external force, and in each case converge to a Gaussian distribution

$$p(x,t) = \frac{1}{\sqrt{2\pi\sigma^2}}\exp\left[-\frac{(x-\mu)^2}{2\sigma^2}\right]. \quad \text{(S11)}$$

In the absence of force, $\mu = 0$ and $\sigma^2 = 2Dt$, where D is the diffusion coefficient. In the presence of a constant external force, F, the force causes the molecule to move with constant velocity $v = F/\gamma$, where γ is the drag coefficient. This drift velocity is superimposed on the diffusive motion such that only the mean is affected and is given by $\mu = vt = (F/\gamma)t$. To test whether our simulation obeyed Eq. S10, we used our modified MMC to simulate molecular diffusion in one dimension with $D = D_{avg}$ (from Eq. S9) in the absence and presence of a constant external force $F = 2$ pN (Figure S1A and B). As shown in Fig. S1A and B, our simulation results fit well with theoretical expectation (from Eq. S11) at multiple time scales and were comparable to those using previous MMC methods.

Since we assume the interaction potential between binding partners is harmonic, we further sought to examine whether our modified MMC algorithm agreed with expectation for diffusion in a harmonic potential, $U(x) = ½kx^2$ where k is the spring constant. Assuming a delta function initial condition, as above, molecular motion obeys an Ornstein-Uhlenbeck process (10), in which the analytical solution to Eq. S10 is

$$p(x,t) = \left(\frac{k}{2\pi k_B T(1-\exp[-(2k/\gamma)t])}\right)^{1/2} \exp\left[-\left(\frac{k}{2k_B T}\right)\frac{\left(x - x_0\exp[-(k/\gamma)t]\right)^2}{\left(1-\exp[-(2k/\gamma)t]\right)}\right]. \quad \text{(S12)}$$

As shown in Fig. S1B and C our modified MMC algorithm agrees with Eq. S12 in both cases where $x_0 = 0$ and $x_0 = 0.2$ nm using $k = k_{\text{long,i}}$. Comparing Eq. S12 to Eq. S11 we can see that in a harmonic potential the resulting distribution is also Gaussian, where the mean and variance are both a function of time

$$\mu(t) = x_0\exp[-(k/\gamma)t] \quad \text{(S13)}$$

$$\sigma^2(t) = \left(\frac{k_B T}{k}\right)\left(1-\exp[-(2k/\gamma)t]\right) \quad \text{(S14)}$$

As $t \to \infty$, Eq. S12 is equivalent to Boltzmann's law ($p \sim e^{-U/k_B T}$) for a harmonic with $U(x) = ½kx^2$

$$p(x, t\to\infty) = \left(\frac{k}{2\pi k_B T}\right)^{1/2} \exp\left[-\left(\frac{k}{2k_B T}\right)x^2\right]. \quad \text{(S15)}$$

At steady-state, $\mu(t\to\infty) = 0$ and $\sigma^2(t\to\infty) = k_B T/k$, which is consistent with equipartition of energy. The mean and variance of particle position converge to steady-state with time constant $\tau = \gamma/k$ and $\tau = \gamma/(2k)$ for the mean and variance, respectively. By estimating the mean and variance of molecule positions as a function of time for the case where $x_0 = 0.2$ nm, we found that our modified MMC algorithm approached steady-state on the correct time scale (Fig. S1D and E). As our algorithm agrees with theoretical expectation in various conditions of diffusion in the absence and presence of force and in steady-state and in unsteady-state, we conclude that it is a good approximation to the equations of diffusive motion.

While our results do not differ from previous methods, our modified MMC approach has several advantages over the previous methods. First, in sampling from a uniform distribution, multiple moves are required before the distribution converges to a Gaussian (via the central limit theorem), compared to our approach where moves for every time step are Gaussian distributed. Therefore, at short time scales (i.e. after few steps) our modified MMC should more accurately predict the expected molecule distribution. Other Brownian dynamics methods have sampled moves from a Gaussian, but assume that the force is constant for each step and therefore is implemented as a drift term (11). Under the simulation conditions used here, we found that results using this method did not differ from our modified MMC (< 5% difference). The assumption that force is constant, however, would break down for steep interaction potentials (i.e. stiff bonds), possibly resulting in quicker transitions to steady-state (Eq. S13 and S14) or quicker escape time from the potential well (unbinding). Additionally, when simulating few diffusing molecules of interest, our algorithm allows the mean squared step size to be scaled to the relative separation between molecules (Eq. S6), so that computational time is not wasted taking small steps ([-r,r]) while molecules are far away from their binding partner.

Influence of hydrodynamic interactions on stereospecific binding in linear polymers

As two Brownian particles approach each other or as a particle approaches a wall, the solvent between them must be forced out, resulting in an increased drag force upon approach (12). In the absence of inter-particle interaction potential, these hydrodynamic interactions reduce the diffusion-limited rate of encounters by ~30% (13, 14). In the presence of an interaction potential, hydrodynamic interactions induce correlation between the movements of nearby molecules, increasing the translational diffusion coefficient while reducing rotational diffusion (11). Thus, it seems that it might be important to include these interactions in any kinetic simulation. In the model described here, freely diffusing subunits bind to sites at the end of the microtubule lattice, which can be thought of as immobile compared to the freely diffusing subunit. Hydrodynamic interactions between the free subunit and the lattice, therefore, will be similar to a particle approaching a wall as described by (12). In this case, hydrodynamic interactions result in a distance dependent effect on the fluid viscosity, η. Therefore, we sought to examine the expected effects of fluid viscosity on the resulting kinetic rate constants.

When considering stereospecific-binding interactions, one must consider both the rate at which molecules collide as well as whether they are properly aligned upon collision. If not initially aligned properly, binding partners can explore additional configurations through rotational diffusion during a single encounter, thereby promoting binding (6). Thus, the efficiency of binding will be dependent on the duration of the encounter and the extent of rotational diffusion during a single encounter

$$\phi = \frac{\left\langle \Delta\theta^2 \right\rangle^{1/2}}{2\pi} = \frac{(2D_{\mathrm{r}}\tau_{\mathrm{E}})^{1/2}}{2\pi} \tag{S16}$$

$$\tau_{\mathrm{E}} = \frac{\delta^2}{6D_{\mathrm{t}}} \tag{S17}$$

where ϕ is the binding efficiency, δ is the encounter distance, and D_{r} and D_{t} are the rotational and translational diffusion coefficients, respectively. Using our model parameters in Eqs. S16-S17, assuming $D_{\mathrm{t}} = D_{\mathrm{avg}}$ and $\delta = 2r_{\mathrm{B}}$, we estimate $\phi = 0.025$, which is nearly identical to that resulting for $N = 1$ (purely diffusive motion) in our simulation (Fig. 3A). Predicting how the binding efficiency will scale with viscosity, η, we see

$$\phi = \frac{(2D_{\mathrm{r}}\tau_{\mathrm{E}})^{1/2}}{2\pi} \propto \left(\frac{D_{\mathrm{r}}}{D_{\mathrm{t}}}\right)^{1/2} \propto \left(\frac{\frac{1}{\eta}}{\frac{1}{\eta}}\right)^{1/2} \tag{S18}$$

Increased viscosity results in a longer encounter but also slows rotational diffusion, and therefore the binding efficiency does not depend upon the viscosity. Assuming the association rate constant is the diffusion-limited collision rate (Smoluchowski rate from Eq. S8) scaled by the binding efficiency

$$k_{\mathrm{on}} = \phi k_{\mathrm{D}} \propto (\text{const.})\frac{1}{\eta} \tag{S19}$$

Thus, the net-effect of hydrodynamic interactions on the rate constant will be equivalent to reduction in diffusion-limited collisions due to distance dependent changes in the viscosity. As noted above, this is predicted to be ~30% reduction for two-spheres (13, 14). Therefore, we predict that incorporating hydrodynamic interactions will reduce the estimated values for the on-rate constant, however, will not influence the binding efficiency of individual subunits. As the

effects of global and local structures at the end of the microtubule are due to the binding efficiency (Fig. 3 and 4) and not due to the translational diffusional approach to a position close to the binding site (i.e. 10 nm in the present study), we have ignored explicit inclusion of hydrodynamic interactions in the results presented here. Instead, the simulation results can be corrected by ~30% to provide more accurate estimates of association rate constants.

Establishing upper and lower bounds for the total longitudinal bond energy

Due to the way that we have modeled bond zone interactions, negative displacements away from the potential minimum ($x = 0$), which result in overlap of super-ellipsoid surfaces, are not allowed. Therefore, we can think of each bound zone as a thermally driven spring where only positive displacements are allowed. The intrinsic bond energy will be related to the total longitudinal bond energy (potential energy well-depth) by

$$U_{\text{long}} = \Delta G_{\text{B}}^{0} - 3U_{\text{i}}(\mu) \tag{S20}$$

where $U_{\text{i}}(\mu)$ is the individual spring potential at the mean position, μ, and ΔG^{0}_{B} is the intrinsic bond strength of the longitudinal bond. If we consider the standard free energy of the longitudinal bond, $\Delta G^{0}_{\text{long}}$, as the difference between the favorable ΔG^{0}_{B} and unfavorable entropic penalty of binding, ΔG^{0}_{S}, then we can substitute for ΔG^{0}_{B} in Eq. S20 to get

$$U_{\text{long}} = \Delta G_{\text{long}}^{0} - \Delta G_{\text{S}}^{0} - 3U_{\text{i}}(\mu) \tag{S21}$$

The mean position of the constrained, thermally driven spring is

$$\mu = \int_{0}^{\infty} x \cdot f(x) \cdot dx = \frac{2}{\sqrt{2\pi\sigma^{2}}} \int_{0}^{\infty} x \cdot e^{-x^{2}/2\sigma^{2}} dx \,, \tag{S22}$$

where the factor of two in the numerator is used to scale the area under the curve to unity. Integration of Eq. S22 results in a mean position of

$$\mu = \frac{2\sigma}{\sqrt{2\pi}} \tag{S23}$$

If we assume that spring displacements have three degrees of freedom, then from equipartition of energy we get $\sigma^{2} = 3k_{\text{B}}T/k_{\text{long,i}}$. Inserting this into Eq. S23, results in a mean position of

$$\mu = \left(\frac{6k_{\text{B}}T}{\pi k_{\text{long,i}}} \right)^{1/2} \tag{S24}$$

and the energy at this position is

$$U_{\text{i}}(\mu) = \frac{1}{2} k_{\text{long,i}} \left(\frac{6k_{\text{B}}T}{\pi k_{\text{long,i}}} \right) = \frac{3k_{\text{B}}T}{\pi} \,. \tag{S25}$$

Therefore, we assume an unfavorable contribution to U_{bond} of ~1 $k_{\text{B}}T$ per interaction zone. Estimates of ΔG^{0}_{S} range from about 10-12 $k_{\text{B}}T$ (15–17), therefore using $\Delta G^{0}_{\text{long}}$ = -6.8 $k_{\text{B}}T$ from (8) we predict that U_{long} = -21.8-19.8 $k_{\text{B}}T$. As shown in Fig. 6C, we find that U_{long} = -20.4 $k_{\text{B}}T$ results in $\Delta G^{0}_{\text{long}}$ = -6.8 $k_{\text{B}}T$.

Sensitivity of model predictions to the interaction potential

To explore whether or not our results were specific to the specific shape of the harmonic potential of interaction, we simulated subunit binding and unbinding using a Lennard-Jones (LJ) interaction potential where the interaction energy for an individual zone was given by

$$U_i(t_j) = -U_{long,i}\left[\left(\frac{r_m}{r_m + r_i(t_j)}\right)^{12} - 2\left(\frac{r_m}{r_m + r_i(t_j)}\right)^{6}\right] \text{ for } r_i(t_j) > 0 \quad \text{(S26)}$$

Here r_m is the distance at which $U_i = U_{long,i}$ and $r_m = 2^{1/6}\sigma$, where σ is a shape parameter that defines the slope of the function for a given value of $U_{long,i}$, similar to the harmonic spring constant. We added r_m to the denominator since r_i is the distance between two points on the surface of the subunits. This ensured that $U_i = U_{long,i}$ when $r_i = 0$. The repulsive portion of the LJ potential for $r_i < r_m$ was maintained by hard-sphere rejection. For simulations using a LJ potential, we defined r_B as the point where the slope, or equivalently the inter-particle force, was at its maximum value.

As shown in Fig. S5, the predicted kinetic and thermodynamic trends for LJ are similar to those predicted using a harmonic potential (Fig. 6 and S4). Stronger bonds (more negative U_{long}) resulted in higher $k_{on,PF}$, lower k_{off}, and thus a more favorable interaction (more negative ΔG^0_{long}). The same trend was observed for softer bonds (more positive shape parameter, σ). Unlike the harmonic potential, we found the estimated entropic penalty of binding (ΔG^0_S) was sensitive to the total bond energy of the LJ. This is because for constant σ, the slope of the LJ potential becomes steeper for more negative values of U_{long}. In contrast, the slope of the harmonic potential is only sensitive to the bond stiffness, k_{long}. Thus, more negative values of U_{long} in the LJ potential also effectively stiffen the bond. When considering this, the trend in ΔG^0_S with regards to bond stiffness is equivalent to that observed for a harmonic potential. In the absence of lateral neighbors, we found that using U_{long} = -30 k_BT and σ = 0.6 nm resulted in $\Delta G^0_{long} \approx$ -6.8 k_BT, and therefore used these values in all subsequent simulations. As shown in Fig. S6, the estimated on-rate constant was slightly lower using a LJ potential for each local condition, however, the steric penalties imposed by local structure were the same as estimated for a harmonic.

In addition to the shape of the potential, it is possible that the parameters used to define the harmonic potential may reduce the steric penalty imposed by laterally adjacent protofilaments. In particular, increasing the bond stiffness would increase the inter-particle force and may help to align subunits in the one and two neighbor case. Alternatively, softer bonds may be able to interact for a longer period of time, while the subunit aligns with the neighboring protofilaments. Therefore, we estimated the penalties for varying longitudinal bond stiffness. While the bond stiffness affected both the estimated on-rate constant and the off-rate constant (Fig. S4), there was no significant effect on the penalties imposed by either one or two lateral neighbors (Fig. S6C and D). These results indicate that the absolute value of the model estimated values depend upon the shape of the chosen potential as well as the parameters that describe it, however, the kinetic rate penalties as well as the kinetic and thermodynamic trends are robust and relatively insensitive to the particular mathematical form of the attractive potential.

Supporting References:

1. Doi, M., and S.F. Edwards. 1986. The Theory of Polymer Dynamics. New York: Oxford University Press.

2. Fernandes, M.X., and J.G. de la Torre. 2002. Brownian dynamics simulation of rigid particles of arbitrary shape in external fields. Biophysical Journal. 83: 3039–48.

3. Metropolis, N., A.W. Rosenbluth, M.N. Rosenbluth, A.H. Teller, and E. Teller. 1953. Equation of State Calculations by Fast Computing Machines. The Journal of Chemical Physics. 21: 1087.

4. Kikuchi, K., M. Yoshida, T. Maekawa, and H. Watanabe. 1991. Metropolis Monte Carlo method as a numerical technique to solve the Fokker—Planck equation. Chemical Physics Letters. 185: 335–338.

5. Tiana, G., L. Sutto, and R.A. Broglia. 2007. Use of the Metropolis algorithm to simulate the dynamics of protein chains. Physica A: Statistical Mechanics and its Applications. 380: 241–249.

6. Northrup, S.H., and H.P. Erickson. 1992. Kinetics of protein-protein association explained by Brownian dynamics computer simulation. Proceedings of the National Academy of Sciences of the United States of America. 89: 3338–42.

7. Andrews, S.S., and D. Bray. 2004. Stochastic simulation of chemical reactions with spatial resolution and single molecule detail. Physical Biology. 1: 137–51.

8. VanBuren, V., D.J. Odde, and L. Cassimeris. 2002. Estimates of lateral and longitudinal bond energies within the microtubule lattice. Proceedings of the National Academy of Sciences of the United States of America. 99: 6035–40.

9. Gardner, M.K., B.D. Charlebois, I.M. Jánosi, J. Howard, A.J. Hunt, et al. 2011. Rapid microtubule self-assembly kinetics. Cell. 146: 582–92.

10. Uhlenbeck, G., and L. Ornstein. 1930. On the Theory of the Brownian Motion. Physical Review. 36: 823–841.

11. Ermak, D., and J. McCammon. 1978. Brownian dynamics with hydrodynamic interactions. The Journal of Chemical Physics. 69: 1352.

12. Brenner, H. 1961. The slow motion of a sphere through a viscous fluid towards a plane surface. Chemical Engineering Science. 16: 242–251.

13. Wolynes, P.G., and J.A. McCammon. 1977. Hydrodynamic Effect on the Coagulation of Porous Biopolymers. Macromolecules. 10: 86–87.

14. Wolynes, P.G. 1976. Slip boundary conditions and the hydrodynamic effect on diffusion controlled reactions. The Journal of Chemical Physics. 65: 450.

15. Erickson, H.P., and D. Pantaloni. 1981. The role of subunit entropy in cooperative assembly. Nucleation of microtubules and other two-dimensional polymers. Biophysical Journal. 34: 293–309.

16. Erickson, H.P. 1989. Co-operativity in protein-protein association. The structure and stability of the actin filament. Journal of Molecular Biology. 206: 465–74.

17. Horton, N., and M. Lewis. 1992. Calculation of the free energy of association for protein complexes. Protein Science. 1: 169–81.

Supporting Movie Descriptions

Movie S1. Subunit binding with zero neighboring protofilaments. Individual runs of subunits that reach R = 10 nm separation distance are shown. Percentages indicate the percent of subunits reaching R = 10 nm that either diffuse away from the lattice (left) or eventually bind (right).

Movie S2. Subunit binding with two neighboring protofilaments. Individual runs of subunits that reach R = 10 nm separation distance are shown. Percentages indicate the percent of subunits reaching R = 10 nm that either diffuse away from the lattice (left) or eventually bind (right).

Movie S3. Bound subunit lifetimes. Bound subunits with zero (left) and one (right) lateral bond are shown. Movie continues until the first subunit leaves the microtubule lattice.

Figure S1

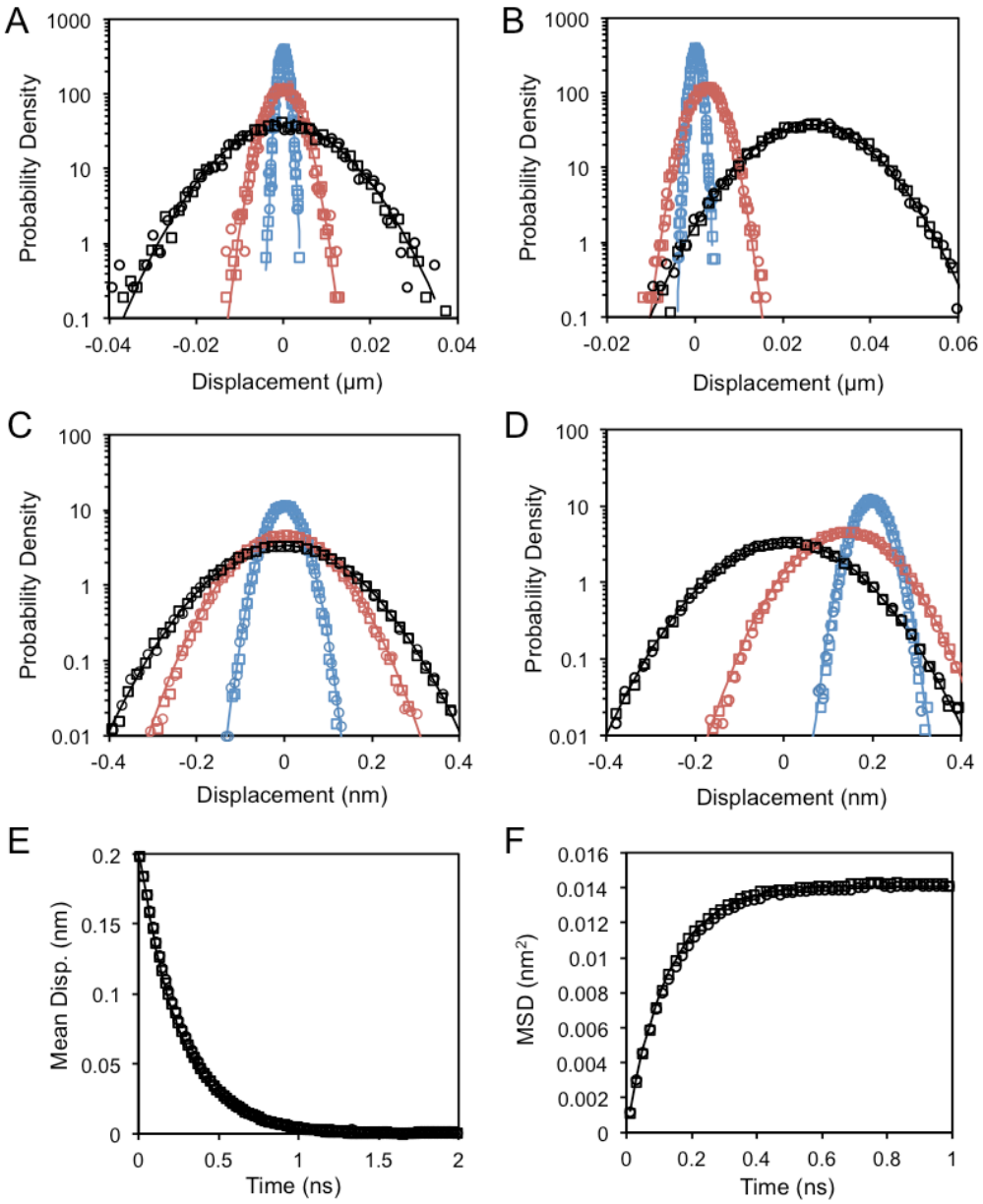

Fig. S1. Comparison of our modified MMC algorithm (circles) to previous MMC methods (squares) as well as theoretical expectation (solid lines). A-B) Resulting probability distributions in the absence (A) and presence (B) of a constant external force at 10 ns (blue), 100 ns (red) and 1 μs (black). In each run $x_0 = 0$. C-D) Probability distributions for diffusion in a harmonic potential where $x_0 = 0$ (C) or $x_0 = 0.2$ nm (D). Distributions were sampled after 10 ps (blue), 100 ps (red), and 1 ns (black). E-F) Starting from $x_0 = 0.2$ nm, the mean displacement (from $x = 0$, E) and the mean-squared displacement (F) were calculated at regular intervals in order to estimate the transition to the predicted steady-state distribution. Theoretical expectation (solid lines) was calculated from Eq. S11 (A and B), Eq. S12 (C and D), Eq. S13 (E), or Eq. S14 (F).

Figure S2

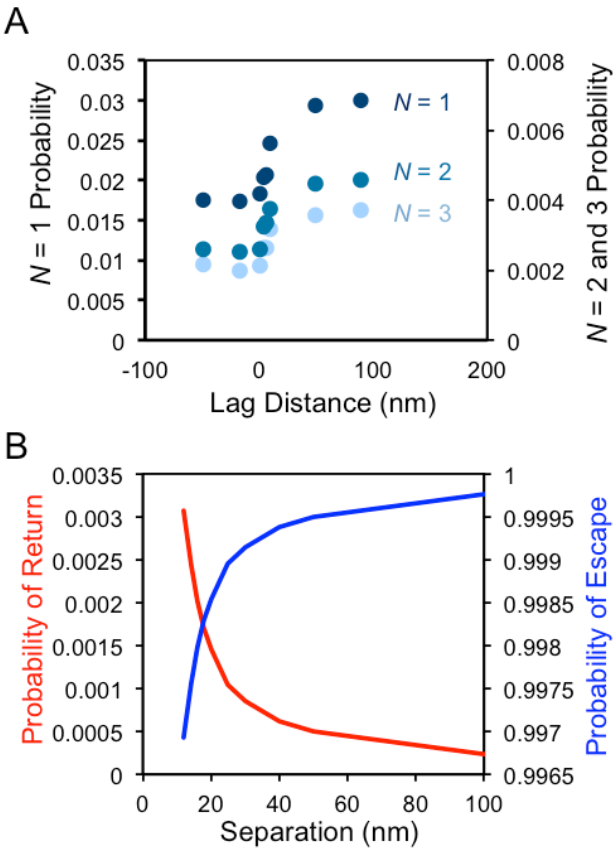

Fig. S2. A) Probabilities of reaching $N = 1$, 2, or 3 zones within the binding radius for binding simulations where the centroid starting position was randomly selected from points along a sphere with radius $R = 10$ nm, centered at the centroid of the subunit of interest in the microtubule lattice. Randomization eliminated any potential spatial bias in the positions of diffusive arrivals. Similar to the trend seen for non-randomized starting positions, free subunits bind more efficiently to lagging protofilaments compared to leading. B) The probability of escaping (diffusing away before binding, blue line) and the probability of return (to $R = 10$ nm separation, red line) as a function of center-to-center separation distance. The probability of escape rapidly increases with separation distance within the range equal to the diameter of the microtubule (~25 nm), suggesting that the longer protofilaments could enhance binding to lagging protofilaments by inhibiting escape.

Figure S3

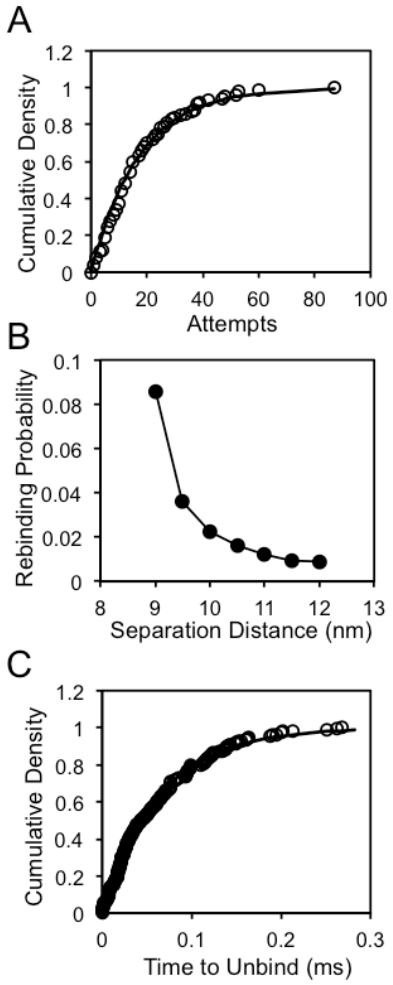

Fig. S3. A) Cumulative density function of the number of times that bound subunits reach the $N = 0$ (all zones separated by greater than the binding radius) state prior to diffusing to a center-to-center distance of $R = 11$ nm. The line is best fit of a geometric distribution (Kolmogorov-Smirnov test, $p > 0.05$), with mean $\mu = 17.7$. The fit of the a geometric distribution indicates that a subunit has an escape probability of 0.06 ($P = 1/\mu$) or 94% chance of rebinding each occurrence of $N = 0$. B) The probability that a subunit completely rebinds ($N = 3$) before diffusing away to a 400 nm center-to center distance as a function of the subunit separation distance. Because diffusing subunits maintain rotational correlation between $N = 0$ and the unbinding distance, units are more likely to rebind compared to a random orientation. The probability decreases the further a subunit is allowed to separate from the protofilament of interest. We defined the unbinding distance by the separation where the probability of rebinding decayed to < 0.01, which was around 11 nm. As the minimum attainable center-to-center distance of bound units is 8 nm, units diffuse ~3 nm before being considered unbound. C) Cumulative density function of the times from the point of first complete binding ($N = 3$) to return to a separation of $R = 11$ nm. Using this distance criterion for unbinding, the unbinding times fit with the expected exponential distribution, fit line, (Kolmogorov-Smirnov test, $p = 0.82$) for a first-order rate.

Figure S4

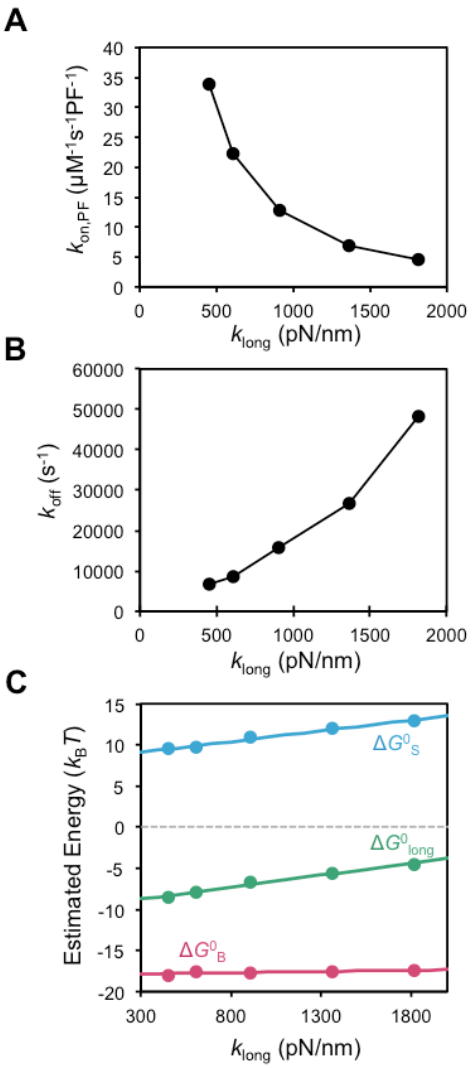

Fig. S4. Kinetic and thermodynamic estimates for longitudinal bonds of varying stiffness are shown. Estimated on-rate constant (A) and off-rate (B) as a function of the stiffness of the longitudinal bond. All simulations are longitudinal bond only with constant total bond energy (U_{long} = -20.4 k_BT). C) The standard free energy (ΔG^0_{long}, green), intrinsic bond strength (ΔG^0_B, magenta) and entropic penalty of binding (ΔG^0_S, blue) are shown as a function of the longitudinal bond stiffness. All trend lines are linear best fit.

Figure S5

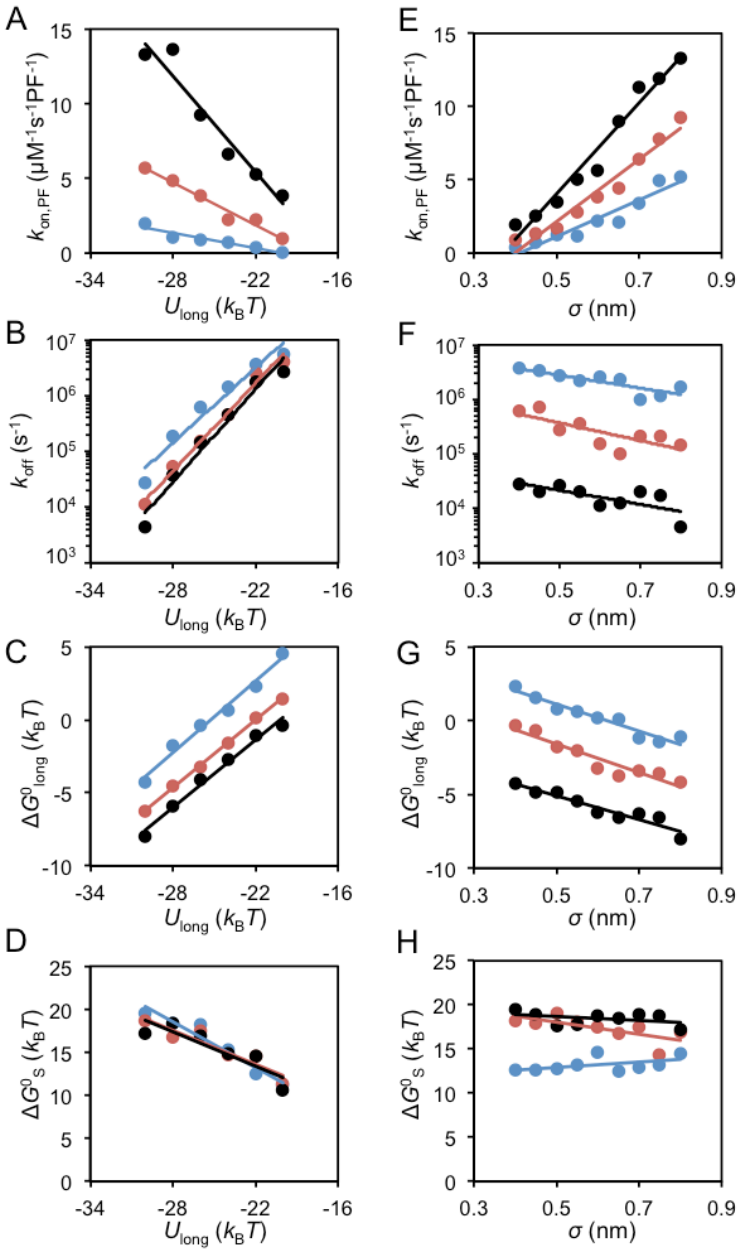

Fig. S5. Kinetic and thermodynamic trends with varying U_{long} (left) and σ (right) used to define the Lennard-Jones potential. For each condition 100,000 near-field binding runs and 10 unbinding runs were performed. A-D) For each value of U_{long}, σ = 0.4 nm (blue), 0.6 nm (red), or 0.8 nm (black). E-H) For each value of σ, U_{long} = -22 k_BT (blue), -26 k_BT (red), or -30 k_BT (black). We found that using U_{long} = -30 k_BT and σ = 0.6 nm resulted in $\Delta G^0_{long} \approx$ -6.8 k_BT, therefore these values were used to estimated $k_{on,PF}$ and the on-rate penalties for each local condition. All trend lines are linear best fit, except for k_{off} which is exponential.

Figure S6

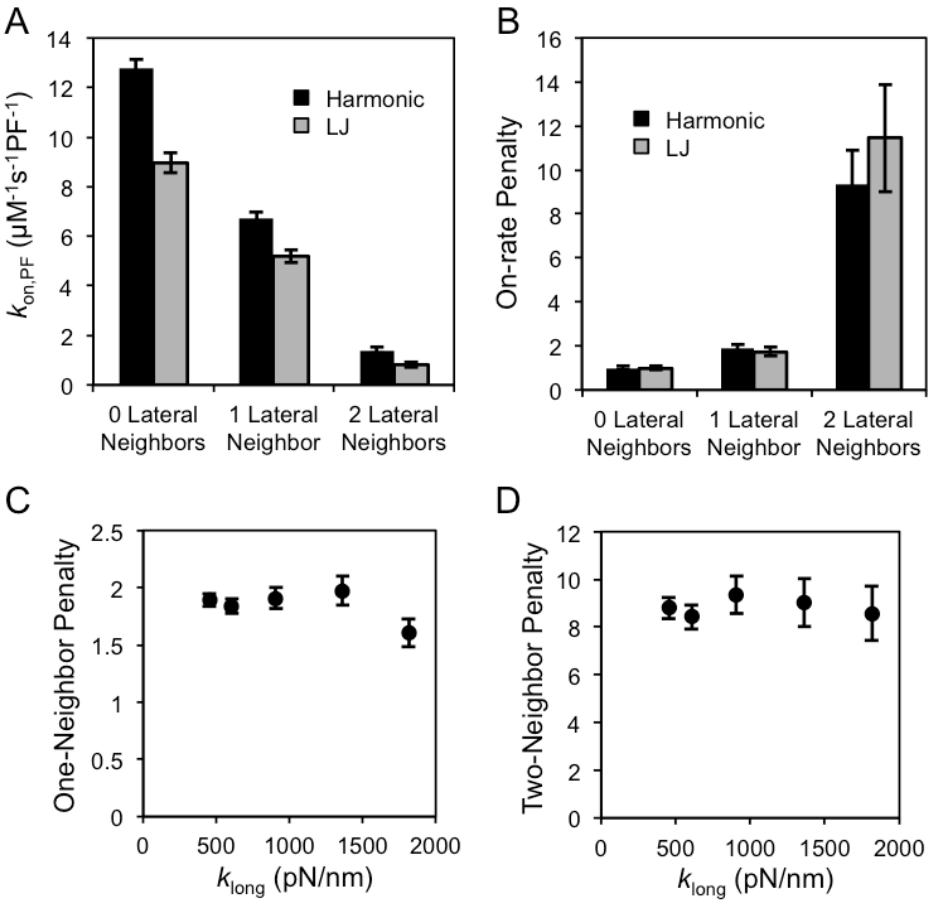

Fig. S6. A) Estimated on-rate constants in each local condition are shown when modeling the interaction potential as a harmonic or Lennard-Jones potential (LJ). Parameters for LJ potential were fit such that ΔG^0_{long} was equal to that using the harmonic. B) On-rate penalties for different potential shapes in each local condition. One-neighbor (C) and two-neighbor (D) on-rate penalties for a range of longitudinal bond stiffness values (harmonic spring constant). While the on-rate estimates are sensitive to the bond stiffness (Fig. 7A), the on-rate penalties are independent of the bond stiffness. All error bars are 95% confidence interval.

Supporting Tables

Table S1 – Model estimated kinetics and thermodynamics for F-actin.

	Leading PF 0 LN	Lagging PF ½ LN	Lagging PF 1 LN
$k_{on,\mathrm{PF}}$ ($\mu M^{-1}s^{-1}PF^{-1}$)	13.7	10.7	9.4
k_{off} (s^{-1})	35 x 10^3	320	< 42
ΔG^0_{B} ($k_{\mathrm{B}}T$)	-16.1	-21.5	-28.5
ΔG^0 ($k_{\mathrm{B}}T$)	-6.0	-10.4	< -12.3
ΔG^0_{S} ($k_{\mathrm{B}}T$)	+10.1	+11.1	< +16.2

Table S2 – Summary of simulation results with lateral bond only.

	Lateral Bond Only, no Longitudinal Bond	
	1 Lateral Neighbor	2 Lateral Neighbors
$k_{on,\mathrm{PF}}$ ($\mu M^{-1}s^{-1}PF^{-1}$)	0.15	0.10
k_{off} (s^{-1})	10^7	7 x 10^6
ΔG^0_{B} ($k_{\mathrm{B}}T$)	-0.44	-3.4
ΔG^0 ($k_{\mathrm{B}}T$)	+4.4	+4.3
ΔG^0_{S} ($k_{\mathrm{B}}T$)	+4.8	+7.7